RESEARCH ARTICLE

A Molecular-Splicing Strategy for Constructing a Near-Infrared Fluorescent Probe for UDP-Glucuronosyltransferase 1A1

Xiangge Tian, [a,b,†] Tao Liu, [c,†] Yinhua Ma, [d,†] Jian Gao, [b] Lei Feng,*, [a, e] Jingnan Cui, [c] Tony D. James, [e, f] and Xiaochi Ma*, [a,b]

Abstract: UDP-glucuronosyltransferase 1A1 (UGT1A1) is a vital metabolic enzyme responsible for clearance of endogenous substances and drugs. Hitherto, the development of fluorescent probes for UGTs was severely restricted due to the poor isoform selectivity, on-off or blue-shifted fluorescence response. Herein, we established a novel "molecular-splicing strategy" to construct a highly selective near-infrared (NIR) fluorescent probe **HHC** for UGT1A1, which exhibited a NIR signal at 720 nm after UGT1A1 metabolism. **HHC** was then successfully used for the real-time imaging of endogenous UGT1A1 in living cells and animals, and to monitor the bile excretion function. In summary, an isoform-specific NIR fluorescent probe has been developed for monitoring UGT1A1 activity in living systems, high-throughput screening of novel UGT1A1 inhibitors and visual evaluation of bile excretion function. This practical "molecular-splicing strategy" is particularly powerful in developing highly selective and enzyme-activated fluorescent probes.

UDP-Glucuronosyltransferases (UGTs) are a major phase II metabolic enzyme family responsible for transferring glucuronic acid to hydrophobic compounds including various endogenous and exogenous substrates in the presence of UDP-glucuronic acid (UDPGA) [1]. In humans, approximately 40–70% of clinical drugs can be metabolized by UGT-mediated glucuronidation. Usually, the water solubility of glucuronic metabolites could promote their excretion from the liver cells by efflux transporters (e.g. breast cancer resistant protein, BCRP), and excreted as bile or urine [2]. To date, three subfamilies of human UGTs including UGT1, UGT2 and UGT3 have been identified, most of which are expressed in the liver (an important tissue for the detoxification of xenobiotics) while some isoforms of UGTs are expressed in extrahepatic tissues such as the intestine, lung and kidney [1, 3].

In humans, UGT1A1, UGT1A3, UGT1A4, UGT1A6, UGT1A9, UGT2B4, UGT2B7, UGT2B10, UGT2B15 and UGT2B17 are extensively expressed in the liver [3-4]. Amongst them, UGT1A1 has attracted significant attention due to its critical role in the conjugative detoxification of bilirubin, the endogenous and toxic by-product of heme metabolism. The metabolic dysfunction of UGT1A1 results in accumulation of bilirubin *in vivo*, which induces jaundice, hyperbilirubinemia or other liver damage [5]. Additionally, recent studies have clearly indicated that UGT1A1 has a close relationship with neonatal and drug-induced jaundice[5c]. Additionally, it also plays an important role in the inactivation and detoxification of clinical drugs, notably, it has been shown that gene polymorphism and individual differences are associated with the side effects and therapeutic efficacy of irinotecan *in clinic* [6]. Thus, the dynamic monitoring of endogenous UGT1A1 activity in various biological systems, is essential for the diagnosis and therapy of UGT1A1-related diseases and the provision of important guidance for the rational use of clinical drugs.

Based on LC-MS/MS analysis, bilirubin has been previously determined as a selective substrate of UGT1A1 [7], however, the instability and photodecomposition of bilirubin restricts its application in detection of UGT1A1 activity within biological specimens. With the development of fluorescence-based technologies, the many advantages including high sensitivity [8], real-time detection, excellent spatiotemporal resolution and non-invasiveness as well as high-throughput screening capacity, have provided a route to break the bottleneck associated with traditional assay methods [9]. As such fluorescence has been widely used to develop enzyme-activated fluorescent probes for the real-time monitoring of enzyme activity [9e, 10], research into biological function [11], medical diagnosis and even intraoperative visualization of various diseases [12].

However, significant challenges have been encountered during the development of selective enzyme-activated fluorescent probes for UGT1A1. Firstly, different subfamilies of UGTs usually share high homology in amino acid sequence (> 65%) such that they exhibit remarkable overlap of substrate specificity. Secondly, the *O*-glucuronidation conjugation reaction of the hydroxyl group of fluorophores is usually accompanied by a blue-shift or on-off change in fluorescence [13]. As such, an efficient strategy for the development of fluorescent probes for UGT1A1 *in vivo* is required. To solve these problems, we propose a novel "molecular-splicing strategy" to construct an enzyme-activated fluorescent probe, which combines the selective recognition site for the target enzyme and fluorescence activatable site of a given fluorophore. Herein, our newly established "molecular-splicing strategy" was used to develop a highly selective NIR fluorescent probe for UGT1A1. Briefly, the optimal metabolic recognition site (5-OH) for

[a] Dr. X. G. Tian, L. Feng, and Prof. X. C. Ma
Second Affiliated Hospital, Dalian Medical University, Dalian 116044, China
E-mail: leifeng@dmu.edu.cn (L. Feng); maxc1978@163.com (X. C. Ma)
[b] Dr. X. G. Tian, J. Gao, and X. C. Ma
Jiangsu Key Laboratory of New Drug Research and Clinical Pharmacy, Xuzhou Medical University, Xuzhou 221004, China
[c] Dr. T. Liu, and Prof. J. N. Cui
State Key Laboratory of Fine Chemicals
Dalian University of Technology
Dalian 116044, China
[d] Dr. Y. H. Ma
Department of Physics
Dalian Maritime University
Dalian 116024, China
[e] Prof. T. D. James, L. Feng
School of Chemistry and Chemical Engineering
Henan Normal University
Xinxiang 453007, China
[f] Prof. T. D. James
Department of Chemistry
University of Bath
Bath BA2 7AY, United Kingdom
[†] These authors contributed equally

Supporting information for this article is given via a link at the end of the document.

UGT1A1 and fluorescent site (6-OH) of the NIR fluorophore hemicyanine (**HC**) were confirmed using *in vitro* metabolic and spectroscopic analysis. The fluorescent site (6-OH) and optimal recognition site (5-OH) were then combined to obtain the target probe (5, 6-diphenol-hemicyanine, **HHC**), which retains the recognition site of UGT1A1. Splicing the 5-OH recognition site with the 6-OH fluorescent site results in non-fluorescent 5,6-diphenol **HHC** ("OFF" splicing). Subsequently, the selective glucuronidation at the 5-OH of **HHC** mediated by UGT1A1 results in **HHC**-5-*β*-D-glucuronoside (**HHC-G**), where the "OFF" splicing effect was remarkably blocked along with the generation of a strong NIR fluorescence signal (Scheme 1). Furthermore, we demonstrate the feasibility and practicability of **HHC** as a molecular tool for monitoring UGT1A1 activity *in vivo*, high-throughput screening of inhibitors, and visual evaluation of bile excretion.

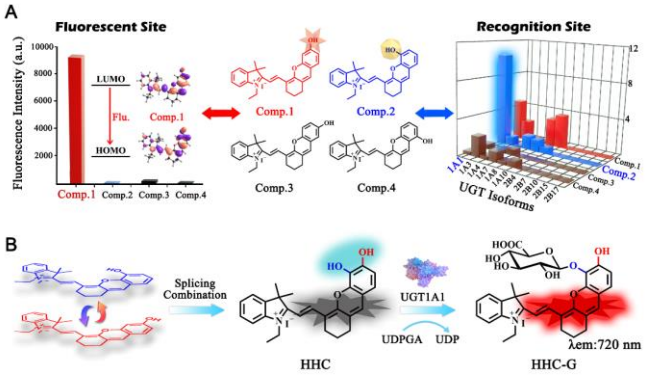

Scheme 1 "Molecular-splicing strategy" for the construction of a selective NIR fluorescent probe for UGT1A1.

In order to investigate the optimum fluorescence site for the NIR fluorophore hemicyanine (**HC**), several compounds with different hydroxyl groups at C-6 (**Comp. 1**), C-5 (**Comp. 2**), C-7 (**Comp. 3**) and C-8 (**Comp. 4**) positions were prepared (Fig. S1). The spectroscopic properties of these compounds are given in Fig. S2 A-B and Fig. S3-S5, the results indicate that only **Comp. 1** exhibits significant fluorescence at 720 nm, while **Comp. 2**-**4** exhibit no fluorescence. Next, the underlying mechanism of the fluorescence properties were determined using DFT/TD-DFT. The optimized ground and excited state geometries of **Comp. 1** are given in Fig. S2C and 2D, and Table S1 summarizes the detailed transition data. For **Comp. 1**, the calculated emission peak (f = 1.3093) is located at 694 nm, which was consistent with our experimental results. The relevant frontier molecular orbitals are shown in Fig. S2E. The emission of **Comp. 1** is mainly composed of LUMO→HOMO, the electron densities of which are both delocalized over the whole molecule, indicating that the S_1 state is a local excited state resulting in strong fluorescence for **Comp. 1**. These results confirm that the fluorescence active site for the hydroxylation reaction of **HC** should be 6-OH.

After determination of the fluorescence active site for **HC**, the metabolic recognition site mediated by UGTs was investigated. As shown in Fig. S6, the UGT isoform-selectivity of **Comp. 1**-**4** was performed among various UGTs isoforms. For **Comp. 1** (6-OH-HC), UGT1A1, 1A3, 1A8 and 1A10 all exhibited a preferable catalytic activity. For **Comp. 3** (7-OH-HC), UGT1A1, 1A3, 1A4, 1A7, 1A8 and 1A10 participated in the glucuronidation reaction, and UGT1A7 exhibited relatively higher catalytic activity. For **Comp. 4** with the hydroxyl group at C-8, both UGT1A3 and 1A7 exhibited higher catalytic activity than the others. Interestingly, for **Comp.2** with 5-OH of **HC**, UGT1A1 exhibited an enhanced selectivity and reaction rate for glucuronidation, with more than 7-22-fold metabolic efficiency than other UGT isoforms, the spectral response toward UGT1A1 is given in Fig. S7. Meanwhile, **Comp. 2** exhibited much higher glucuronidation activity than **Comp. 1**, **3**, and **4** toward UGT1A1 (Fig. S6 E-H). Thus, 5-OH group of **HC** was determined as the best metabolic recognition site for UGT1A1.

In order to rapidly develop the highly selective enzyme-activated fluorescent probe, we employed a design strategy that spliced the recognition site of a given enzyme and fluorescent site of a target fluorophore, "OFF" splicing of substituent groups, to construct an enzyme-activated fluorescent probe. As a case study for our "molecular-splicing strategy" toward UGT1A1; we first confirmed the optimal recognition site (5-OH) of **HC** toward UGT1A1 and fluorescent active site (6-OH) for **HC** (Scheme A), then we combined **Comp. 1** (6-OH-HC, containing the fluorescent active site) and **Comp. 2** (5-OH-HC, containing the recognition site) to obtain 5, 6-diphenol-hemicyanine (**HHC**, **Comp. 5**). Importantly, due to the "OFF" splicing of *O*-diphenol hydroxyl groups, **HHC** produced no fluorescence output, while simultaneously being a favored recognition site (5-OH) for UGT1A1. Then, after glucuronidation at the favored recognition site (5-OH) of **HHC** by UGT1A1 to form **HHC-5-*β*-D-glucuronoside** (**HHC-G**), the "OFF" splicing of the *O*-diphenol was blocked, resulting in the emergence of NIR fluorescence (Scheme B). Thus, **HHC** can be used as a potential off-on NIR fluorescent probe for UGT1A1.

According to the design strategy outlined above, the spectroscopic response of **HHC** toward UGT1A1 was evaluated. As shown in Fig. 1A and 1B, after incubation with UGT1A1, an absorption peak at 690 nm was observed, accompanied by a remarkable fluorescence off−on response at 720 nm, which confirms the suitability of the "molecular-splicing strategy" for **HHC**, (Scheme B). It is worth noting that the metabolic product of **HHC** from UGT1A1 was a mono-glucuronidated product according to LC-HRMS analysis (Fig. S8), the glucuronidation site was identified to be C-5 position using 2D NMR (Fig. S9-S12), which is in accordance with our "molecular-splicing strategy". The spectral properties of **HHC** and **HHC-G** are given in Fig. S13. Next, the underlying mechanism for the fluorescence properties of **HHC** and **HHC-G** was further elucidated. The optimized ground and excited state geometries of **HHC** and **HHC-G** are shown in Fig. S14, and Table S1 summarizes the detailed transition data. Fig. 1C displays the relevant frontier molecular orbitals of **HHC** and **HHC-G**.

For **HHC**, the oscillator strength (f = 0.0199) of the $S_1 \rightarrow S_0$ transition is near zero, indicating that the S_1 state of **HHC** is a forbidden state. It is noted that the electron densities of the HOMO and LUMO are localized on a different part of the **HHC**. Therefore, the first lowest-lying transition undergoes an evident intramolecular charge transfer process, which will induce luminescence quenching of **HHC**. However, after interacting with UGT1A1, the $S_1 \rightarrow S_0$ transition for **HHC-G** is located at 740 nm with the oscillator strength being 0.9853, which corresponds well with the experimental result (720 nm). The larger oscillator strength indicates that the S_1 state of **HHC-G** is a fluorescent state. As shown in Table S1 and Fig. 1C, the $S_1 \rightarrow S_0$ transition corresponds to LUMO→HOMO, with the electron densities localizing on the same molecular moiety. Thus, the strong fluorescence of **HHC-G** should be attributed to the local

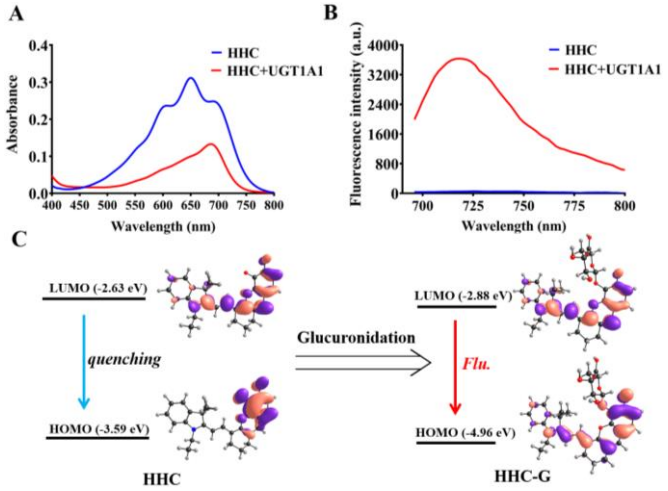

Fig. 1 Absorption (A) and fluorescence (B) spectral response of **HHC** (10 μM) toward UGT1A1, λ_{ex} = 670 nm; (C) calculated HOMO and LUMO molecular orbitals involved in the emission for **HHC** and **HHC-G**.

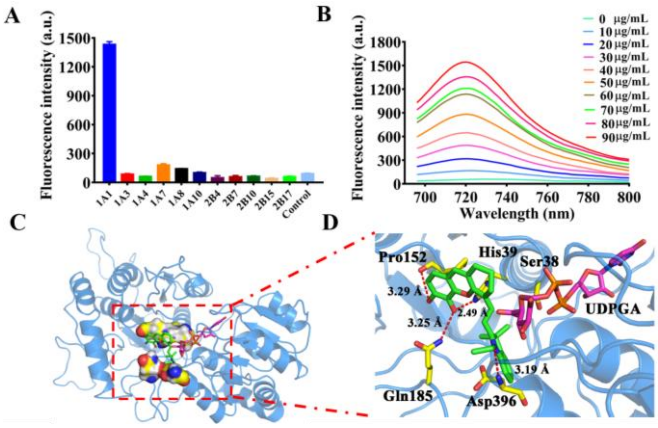

Fig. 2 (A) Selectivity of **HHC** among the various UGTs isoforms; (B) fluorescence intensity changes of **HHC** after incubation with different concentrations of UGT1A1 over a range from 0-90 μg/mL, λ_{ex} = 670 nm; (C) molecular docking of **HHC** and UGT1A1; (D) detailed potential interaction of **HHC** with various critical amino acids in UGT1A1.

excited emission. In summary, all the above results confirm that **HHC** behaves as an off-on NIR fluorescent probe for detecting UGT1A1.

Selectivity toward specific target enzymes has resulted in the extensive utilization of fluorescent probes within complex biological systems. Therefore, to evaluate the selectivity of **HHC**, a panel of human UGT isoforms was used in parallel under the same conditions. As shown in Fig. 2A, among the various UGT isoforms, only UGT1A1 could trigger a fluorescence intensity enhancement, while other UGT isoforms exhibited weak fluorescence response. The formation rates of **HHC-G** mediated by UGT1A1 are 16-fold higher than for other UGTs. Furthermore, the changes of fluorescence intensity exhibited good linear correlation with increasing enzyme concentration of UGT1A1 (r^2 = 0.9935) and different incubation times (Fig. 2B, and S15A).

Additionally, to verify the selectivity of **HHC** toward UGT1A1, chemical inhibition was performed, as shown in Fig. S15B, only UGT1A1 selective inhibitor Neobavaisoflavone (NBF) could block the reaction resulting in residual activity of 15%. The IC_{50} values of NBF inhibited **HHC** glucuronidation in the HLMs (10.43 μM) and UGT1A1 (7.89 μM) systems were similar, which confirms the high selectivity of **HHC** toward UGT1A1 in complex systems (Fig. S15C). Finally, **HHC** was used to assay UGT1A1 activity in 22 individual HLMs, and the results indicated that UGT1A1 activity exhibited a 16-fold difference among different HLMs, due to significant gene polymorphism of UGT1A1 (Fig. S15D).

To elucidate the binding interactions between UGT1A1 and **Comp. 1**, **2** and **HHC**, molecular docking studies were performed using the Surflex docking module in Sybyl X-2.1. The results indicated that all three compounds fitted well into the catalytic cavity of UGT1A1, while the binding modes of the three compounds were somewhat different. In detail, **Comp. 1** forms one hydrogen bond with the side chain of Ser38 in UGT1A1 (Fig. S16A). In addition, the distance between the oxygen atom at C-6 of **Comp. 1** and the nitrogen atom on the imidazole ring of His39 (critical catalytic amino acids in UGT1A1) is 5.72 Å, which results in a lower catalytic activity for **Comp. 1** (Fig. S16A). In contrast, the corresponding distances for **Comp. 2** and **HHC** were 2.70 Å and 2.49 Å (Fig. S16B and Fig. 2C, 2D), respectively; which are a good fit for the catalytic activity. Apart from the residue His39, **Comp. 2** also formed hydrogen bonding interactions with Gln185. Compared to **Comp. 2**, **HHC** exhibited two additional hydrogen bonds with the residues Pro152 and Asp396 (Fig. 2D). The binding affinities of **Comp. 2** and **HHC** to UGT1A1 are stronger than that for **Comp. 1**, which was in accord with the experimental results that **Comp. 2** and **HHC** exhibit higher catalytic efficiency and selectivity for UGT1A1 than **Comp. 1**.

As a practical fluorescent probe, we then explored the fluorescence imaging ability of **HHC** in living cells. Firstly, we determined that **HHC** had no cytotoxicity toward living cells using a CCK8 assay (Fig. S17). As shown in Fig. S18 D-F, after incubating with **HHC**, a significant fluorescence output was detected for the red channel (690 – 750 nm) in HepG2 cells, which indicates the excellent cell permeability of **HHC**, and efficient catalysis mediated by endogenous UGT1A1, while the control group exhibited no fluorescence output (Fig. S18 A-C). The visualization of endogenous UGT1A1 was carried out using LoVo cells (Fig. S18 G-L). Following this **HHC** was evaluated using flow cytometric analysis, as shown in Fig. S19, both the fluorescence signals in HepG2 (A) and LoVo (B) cells exhibited a significantly larger shift than the control group after incubating with **HHC**. To verify the high selectivity of **HHC** toward UGT1A1 in living systems, fluorescence imaging was performed using si-transfected HepG2 cells (genetic ablation of UGT1A1) and control group. As shown in Fig. 3A-H, after pretreating siRNA for knock-down of UGT1A1 in living cells, the fluorescence signal was significantly reduced, and in addition the western blot experiments revealed the down expression of UGT1A1.

Additionally, as shown in Fig. 3 I-P, the UGT1A1 expression levels were upregulated after treatment with UGT1A1 inducer, and the fluorescence signal was significantly enhanced. The changes of fluorescence signal were consistent with the UGT1A1 protein expression in both knockdown and upregulation experiments, which confirmed that the intracellular fluorescence signal was predominantly dependent on the UGT1A1-mediated glucuronidation of **HHC**. Collectively, these results confirm that **HHC** can be used to measure endogenous UGT1A1 activity in a variety of living cells accurately and selectively. Then **HHC** was used to image UGT1A1 in tumor tissue, as shown in Fig. S20, no background fluorescence of control tumor tissue slices was detected (Fig. S20A-C, G-I), yet significant fluorescence was observed in HepG2 (Fig. S20D-F) and LoVo (Fig. S20J-L) cancer tissue slices, respectively. Taken together, these results

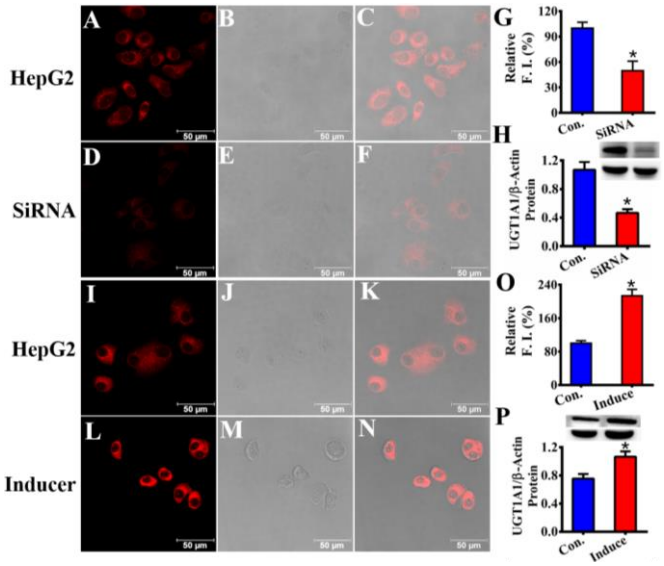

Fig. 3 (A-C) Fluorescence imaging of UGT1A1 in si-transfected HepG2 cells treated with negative SiRNA; (D-F) UGT1A1 imaging after si-transfection by UGT1A1 SiRNA; (G) relative quantification of average fluorescence intensity of UGT1A1 in the control and SiRNA treatment groups; (H) WB assay and grayscale analysis of UGT1A1 expression in the control and SiRNA treatment groups; (I-K) fluorescence imaging of UGT1A1 in HepG2 cells; (L-N) UGT1A1 imaging after induction by rifampin and dexamethasone; (O) relative quantification of average fluorescence intensity of UGT1A1 in the control and induced groups; (P) WB assay and grayscale analysis of UGT1A1 expression for control and induced groups. *P < 0.05.

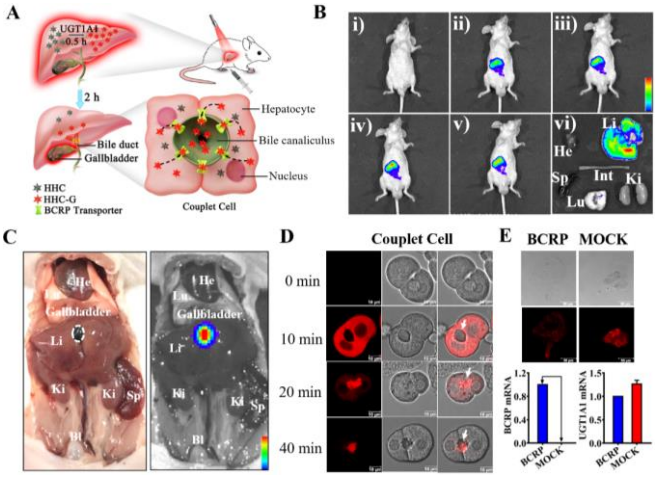

Fig. 4 (A) Graphic description; (B) i-v: *in vivo* imaging of UGT1A1 in live animals after intraperitoneal (i.p.) administration of **HHC** for 0- 30 min and *in vitro* imaging of UGT1A1 in different organs after incubation with **HHC** (10 μM) after 30 min; (C) bright and fluorescence fields for the **HHC** images of the abdominal cavity of mice after i.p. injection of **HHC** at 2 h. He, Heart; Lu, Lung; Gb, gallbladder; Li, liver; Ki, kidney; Sp, spleen Bl, bladder; (D) UGT1A1 imaging in liver couplet cells over 0-40 min; (E) fluorescence imaging of UGT1A1 in BCRP-overexpressed MDCK cells and MOCK cells, and the q-PCR analysis of BCRP and UGT1A1 in these cells.

indicate that **HHC** could be used as a promising tool for monitoring UGT1A1 activity in complex biosystems such as cells and tissues, which could provide useful guidance for surgical diagnosis and the treatment of various cancers *in clinic*.

UGT1A1 is highly expressed in the liver and responsible for the conjugation and detoxification of both endogenous and xenobiotic compounds, especially endogenous bilirubin. Additionally, the glucuronide metabolites of UGT1A1 are readily excreted from the liver *via* bile efflux transporters such as BCRP [2b, 14]. Based on the biological function of UGT1A1, using the distinct “light-up” NIR signal of **HHC**, we evaluated its ability for the real-time visualization of endogenous UGT1A1 in living animals. As shown in Fig. 4A-B, after the administration of **HHC**, significant fluorescence was detected that increased over 30 min, notably, the location of the fluorescence signal was observed in the hepatic area which was the most abundant UGT1A1 expressing organ.

Additionally, the *in vitro* imaging of UGT1A1 in different organs (Heart, Liver, Spleen, Lung, Kidney and Intestine) prepared from the mouse indicated that only the liver exhibited significant fluorescence output, which was consistent with the *in vivo* imaging for live animals (Fig. 4B). Interestingly, after 2 h administration of **HHC**, the fluorescence signal concentrated in the gallbladder (Fig. 4C), which indicated that the glucuronidation metabolite (**HHC-G**) formed in the liver, could be excreted along with bile. The bile containing **HHC-G** flowed directly into the gallbladder, and resulted in an accumulation of NIR fluorescence in the gallbladder. Furthermore, the bile excretion progress was imaged using **HHC** in primary hepatocyte couplet cells. As shown in Fig. 4D, after adding **HHC** to hepatocyte couplets, fluorescence signal variation from 10 min to 40 min was observed. Over the first ten minutes, **HHC** could be metabolized to **HHC-G** by UGT1A1 in hepatic couplet cells, leading to fluorescence distribution in the cytoplasm. Following **HHC-G** efflux from the cytoplasm to the couplet cavity, the fluorescence signal partly transferred into the cavity of the couplet cells. After a long time (40 min), the **HHC-G** completely effluxes to the capillary bile duct, and strong fluorescence could be observed in the cavity of the couplet cells. The real-time fluorescence imaging in liver couplet cells clearly illustrates the excretion progress of **HHC-G**.

In order to confirm whether **HHC-G** was the substrate of BCRP (an important efflux transporter of the bile excretion progress), fluorescence imaging was conducted in BCRP over-expressed and MOCK cell lines (without expression of BCRP) MDCK. As shown in Fig. 4E, the BCRP expression cells displayed lower fluorescence than MOCK cells, due to the excretion of over-expressed BCRP transporter. All these results clearly indicate that **HHC** can be used for the *in vivo* imaging of UGT1A1 in live animals, and **HHC-G** as a glucuronidation metabolite, was a substrate of BCRP transporter. In summary, **HHC** could be used as molecular tool to detect intrahepatic UGT1A1 activity in live animals and monitor the efflux function of the liver *via* bile for the diagnosis of liver related diseases.

Encouraged by the ability of the UGT1A1-activated fluorescent probe (**HHC**) to detect the efflux function of bile, a cholesterol gallstone mouse model was established to evaluate the practicability and reliability of **HHC** for monitoring the efflux function in a gallstone model developed using a bile salt diet induced pathological state. As shown in Fig. 5A-C, after 5 weeks of bile salt diet feeding, stone crystallization was observed in the mice gallbladder by the naked eye and polarized-light microscopy, while the normal diet group exhibited a translucent appearance of the gallbladder without marked gallstone formation. The weight of stone in the cholesterol gallstone group was significantly higher than the normal group and the concentration of total bile acid (TBA) exhibited a dramatic increase in the gallstone model (Fig. 5C). All the results indicated that the bile gallstone model was successfully established.

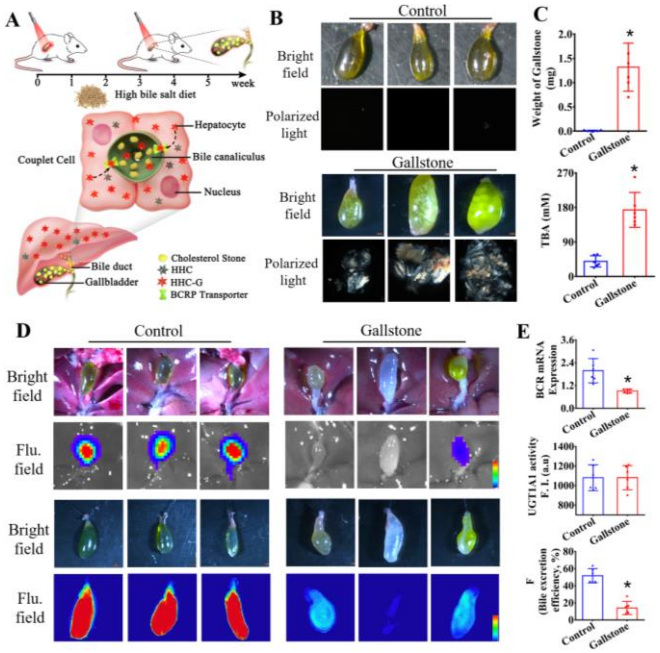

Fig. 5 (A) Graphic description; (B) imaging of gallbladder and polarized light imaging of Control and Gallstone group, respectively; (C) the lithiasis weight and TBA concentration in gallbladder of Control and Gallstone group, respectively; (D) the bright and fluorescence imaging fields for the gallbladder *in vivo* and *in vitro* of Control and Gallstone group, respectively; (E) the mRNA expression of BCRP measured by q-PCR, UGT1A1 activity assayed by **HHC** and "*F*" values (the bile excretion efficiency) for Control and Gallstone group, respectively. *P < 0.01.

Next, **HHC** fluorescence imaging was used to detect the biliary excretion function in the control and gallstone model group. As shown in Fig. 5D, the normal diet group exhibited clear bile and following the administration of **HHC**, significant fluorescence was observed in the gallbladder, however, the gallstone model group displayed a large amount of muddy stone and very weak fluorescence signals in the gallbladder. These results confirmed that the biliary excretion function in a gallstone model was destroyed when compared with that of control mice. Furthermore, to prove the detection accuracy of **HHC**, we analyzed the expression levels of UGT1A1 and BCRP in liver tissue using q-PCR. UGT1A1 expression in the gallstone model exhibited no change but BCRP transporter expression was significantly decreased when compared with the control mice (Fig. 5E). Furthermore, the "*F*" values (representing the bile excretion efficiency, Eq. S1) for the control group were much higher than the gallstone group (Fig. 5E). All these results indicate that the bile gallstone significantly influences the hepatic efflux function. Therefore, the UGT1A1-activated fluorescent probe (**HHC**) could be used as a promising tool for the detection of the biliary excretion function, based on BCRP transporter activity of the capillary bile duct.

It is well-known that UGT1A1 is the unique enzyme during the conjugative detoxification of bilirubin, moreover, it also participates in the detoxification of clinical drugs such as etoposide, SN-38 (the active metabolite of CPT-11), and chemical carcinogens. Thus, the inhibition of UGT1A1 would delay the glucuronidation rates of bilirubin and UGT1A1-substrate drugs enhancing the risks of hyperbilirubinemia and drug-induced liver injury.[4-5] Additionally, the strong inhibition of UGT1A1 may trigger adverse drug/herb–drug interactions[4, 15]. Therefore, both the US Food and Drug Administration (FDA) and European Medicines Agency (EMA) have recommended that the interaction between clinical drugs and UGT1A1 should be assayed [16]. Herein, a high-throughput screening method was developed using **HHC** for the discovery of UGT1A1 inhibitors from herbs. The inhibitory effects of 180 herbs toward UGT1A1 were screened using our high-throughput screening method. From the heat map of inhibition activity (Fig. 6A), *Sophora flavescens Ait.* (M5) [17], a widely used herbal medicine, exhibited significant inhibition toward UGT1A1. Then, 13 fractions of *Sophora flavescens Ait.* were collected (Fig. 6B), and rapidly screened, and the best inhibitory effect was observed for fractions Fr.9-10 (Fig. 6C). Finally, two compounds with inhibitory effect toward UGT1A1 were purified and identified as Kurarinone (**KSC-1**) and Kushenol N (**KSC-3**) (Fig. S21-S24). Subsequently, the inhibitory effects were confirmed using bilirubin as an endogenous substrate of UGT1A1. The inhibition IC_{50} values toward UGT1A1 with different substrates including **HHC** and bilirubin, were calculated to be 0.46 μM and 0.92 μM, for **KSC-1**, respectively; and 0.18 μM and 0.71 μM for **KSC-3**, respectively (Fig. 6D). As such, this research could be used for the *in vitro* investigation of drug metabolism by UGT1A1 during preclinical evaluation, and provided some guidance for the rational use of herbal medicines.

The inhibition of UGT1A1 by **KSC-1** was confirmed using the fluorescence imaging of liver tissue (Fig. 6E). Since, strong inhibition of UGT1A1 usually induces hepatotoxicity *in clinic*, as expected, after orally administration of **KSC-1** for 7 days, Aspartate aminotransferase (AST) displayed a marked increase, however the direct bilirubin (glucuronidation of bilirubin) level exhibited a decrease when compared with the control group, due to the inhibition of UGT1A1 activity by **KSC-1** (Fig. 6F). In H&E staining of liver slices, the hepatocyte exhibited obvious swelling and irregular cell morphology in the **KSC-1** treatment group (Fig. 6G). All these results indicated that **HHC** could be used as a useful tool for the rapid discovery of potential inhibitors of UGT1A1 and provide useful guidance in the rational use of clinical drugs and herbal medicines.

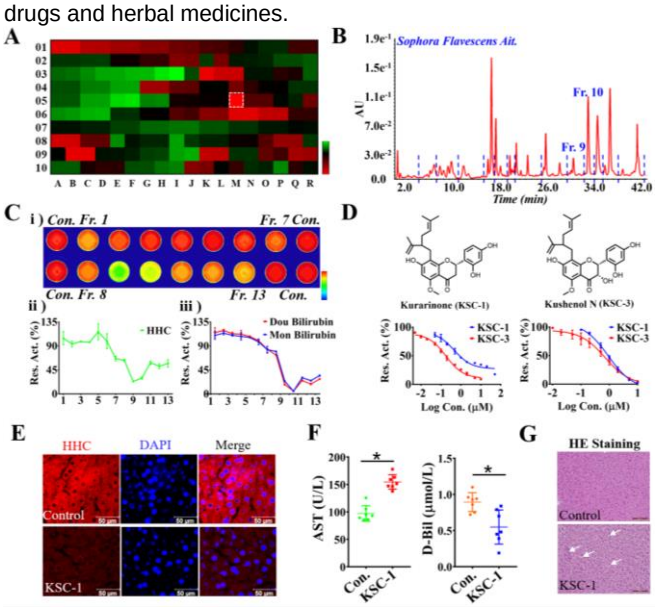

Fig. 6 (A) Visual high-throughput fluorescence image of the inhibitory effects of 180 kinds of herbs toward UGT1A1; (B) HPLC fractions of *Sophora flavescens Ait.* (C) screening of the inhibition activity of fractions toward UGT1A1 using **HHC** as substrate (i: imaged in GE Typhoon FLA9500 with an excitation laser of 633 nm equipped with an emission filter of 720 ± 10 nm; ii: the inhibition activity acquired using Bio-Tek Synergy H1 reader; iii: the inhibition of fractions toward UGT1A1 using bilirubin as substrate, Dou Bilirubin and Mon Bilirubin mean double-glucuronidation and mono-glucuronidation product, respectively; (D)

structures of **KSC-1** and **KSC-3**, and their inhibition IC_{50} curves toward UGT1A1 using **HHC** (left) and bilirubin (right) as substrate; (E) fluorescence imaging UGT1A1 in liver tissue slices for control and preincubated with **KSC-1** groups, respectively; (F) AST and D-Bil analysis for the mice groups including control and treated with **KSC-1** for one week, *P < 0.05; (G) Hematoxylin-Eosin staining in control and **KSC-1** treatment group.

In summary, using a novel "molecular-splicing stratergy", a NIR fluorescent probe **HHC** for UGT1A1 has been developed based on the fluorophore hemicyanine. **HHC** exhibited high selectivity and sensitivity for the real-time detection of UGT1A1 activity. Furthermore, **HHC** could be used for monitoring the bile excretion function of live cells and animal models; and served as a high-throughput screening tool for the rapid discovery of potential inhibitors of UGT1A1, avoiding hepatotoxic risk during clinical medication. Our findings confirm that **HHC** is a promising tool for the diagnosis of UGT1A1-associated diseases and could guide the rational use of clinical drugs, as well as facilitating detailed investigations of the potential biological functions of UGT1A1. Finally, we anticipate that our "molecular-splicing strategy" could be used as an effective method for developing other enzyme-activated and isoform-specific fluorescent probes.

Acknowledgements

The authors thank the National Natural Science Foundation of China (81930112, 82004211 and 82104361), National Key R&D Program of China (2018YFC1705900), Liaoning Provincial Key R&D Program (2019JH2/10300022), Dalian Science and Technology Leading Talents Project (2019RD15) and the open Research Fund of the School of Chemistry and Chemical Engineering, Henan Normal University for support (2020ZD01 and 2021YB07) for financial support, T.D.J. wishes to thank the Royal Society for a Wolfson Research Merit Award.

Conflict of interest

The authors declare no conflict of interest.

Keywords: UDP-glucuronosyltransferase 1A1, NIR fluorescent probe, molecular- splicing strategy, fluorescence imaging.

[1] A. Radominska-Pandya, S. Bratton, J. Little, *Curr. Drug Metab.* **2005**, *6*, 141-160.

[2] a) C. Qi, J. Fu, H. Zhao, H. Xing, D. Dong, B. Wu, *Xenobiotica* **2019**, *49*, 276-283; b) P. Krishnamurthy, J. D. Schuetz, *Annu. Rev. Pharmacol. Toxicol.* **2006**, *46*, 381-410; c) Y. Wei, B. Wu, W. Jiang, T. Yin, X. Jia, S. Basu, G. Yang, M. Hu, *Mol. Pharm.* **2013**, *10*, 1736-1750.

[3] S. Oda, T. Fukami, T. Yokoi, M. Nakajima, *Drug Metab. Pharmacokinet.* **2015**, *30*, 30-51.

[4] T. Kiang, M. Ensom, T. Chang, *Pharmacol. Ther.* **2005**, *106*, 97-132.

[5] a) C. Xu, B. Reck, Z. Xue, L. Huang, K. Baker, M. Chen, E. Chen, H. Ellens, V. Mooser, L. Cardon, C. Spraggs, L. Pandite, *Br. J. Cancer* **2010**, *102*, 1371-1377; b) K. Mazur-Kominek, T. Romanowski, K. Bielawski, B. Kielbratowska, K. Preis, I. Domzalska-Popadiuk, M. Slominska-Fraczek, K. Sznurkowska, J. Renke, K. Plata-Nazar, K. Sledzinska, G. Sikorska-Wisniewska, M. Gora-Gebka, A. Liberek, *Acta Biochim. Pol.* **2017**, *64*, 351-356; c) H. Li, P. Zhang, *J Matern. Fetal. Neonatal. Med.* **2019**, 1-8; d) J. Jordovic, K. Bojovic, J. Simonovic-Babic, V. Gasic, N. Kotur, B. Zukic, M. Vukovic, S. Pavlovic, I. Lazarevic, I. Bekic, N. Nikolic, A. Urosevic, N. Mitrovic, D. Delic, *J. Med. Biochem.* **2019**, *38*, 45-52.

[6] a) C. Tian, H. Ying, R. Zhuang, X. Zhang, H. Lu, H. Wang, S. Wang, Q. Li, C. Wang, X. Cai, *Cancer Manag. Res.* **2018**, *10*, 6217-6226; b) Y. Chen, F. Hu, C. Li, J. Fang, L. Chu, X. Zhang, Q. Xu, *Biomarkers* **2014**, *19*, 56-62; c) Y. Liu, J. Ramirez, L. House, M. J. Ratain, *Eur. J. Cancer* **2010**, *46*, 2097-2103.

[7] S. Putluru, M. Matta, D. Ahire, M. Subramanian, M. Sinz, S. Mandlekar, *Drug Metab. Lett.* **2017**, *10*, 264-269.

[8] a) J. Zhang, X. Chai, X. P. He, H. J. Kim, J. Yoon, H. Tian, *Chem. Soc. Rev.* **2019**, *48*, 683-722; b) X. Wu, W. Shi, X. Li, H. Ma, *Acc Chem. Res.* **2019**, *52*, 1892-1904.

[9] a) X. Tian, F. Yan, J. Zheng, X. Cui, L. Feng, S. Li, L. Jin, T. D. James, X. Ma, *Anal. Chem.* **2019**, *91*, 15840-15845; b) J. Ning, W. Wang, G. Ge, P. Chu, F. Long, Y. Yang, Y. Peng, L. Feng, X. Ma, T. D. James, *Angew Chem. Int. Ed. Engl.* **2019**, *58*, 9959-9963; c) J. Ning, T. Liu, P. Dong, W. Wang, G. Ge, B. Wang, Z. Yu, L. Shi, X. Tian, X. Huo, L. Feng, C. Wang, C. Sun, J. Cui, T. James, X. Ma, *J. Am. Chem. Soc.* **2019**, *141*, 1126-1134; d) L. Feng, J. Ning, X. Tian, C. Wang, L. Zhang, X. Ma, T. James, *Coord. Chem. Rev.* **2019**, *399*, 213026; e) S. H. Gardner, C. J. Reinhardt, J. Chan, *Angew Chem. Int. Ed. Engl.* **2020**; f) T. Terai, T. Nagano, *Pflugers Arch.* **2013**, *465*, 347-359.

[10] J. Huang, J. Li, Y. Lyu, Q. Miao, K. Pu, *Nat. Mater.* **2019**, *18*, 1133-1143.

[11] a) H. W. Liu, L. Chen, C. Xu, Z. Li, H. Zhang, X. B. Zhang, W. Tan, *Chem. Soc. Rev.* **2018**, *47*, 7140-7180; b) H. Li, Q. Yao, W. Sun, K. Shao, Y. Lu, J. Chung, D. Kim, J. Fan, S. Long, J. Du, Y. Li, J. Wang, J. Yoon, X. Peng, *J. Am. Chem. Soc.* **2020**, *142*, 6381-6389.

[12] a) J. Chin, H. Kim, *Coord. Chem. Rev.* **2018**, *354*, 169-181; b) Y. Jin, X. Tian, L. Jin, Y. Cui, T. Liu, Z. Yu, X. Huo, J. Cui, C. Sun, C. Wang, J. Ning, B. Zhang, L. Feng, X. Ma, *Anal. Chem.* **2018**, *90*, 3276-3283; c) G. A. Casay, T. Czuppon, J. Lipowski, G. Patonay, *Proc. SPIE-Int. Soc. Opt. Eng.* **1993**, *1885*, 324-336; d) J. Zhou, P. Jangili, S. Son, M. S. Ji, M. Won, J. S. Kim, *Adv. Mater.* **2020**, *32*, e2001945.

[13] a) X. Lv, G. Ge, L. Feng, J. Troberg, L. Hu, J. Hou, H. Cheng, P. Wang, Z. Liu, M. Finel, J. Cui, L. Yang, *Biosens. Bioelectron.* **2015**, *72*, 261-267; b) T. Terai, R. Tomiyasu, T. Ota, T. Ueno, T. Komatsu, K. Hanaoka, Y. Urano, T. Nagano, *Chem. Commun.* **2013**, *49*, 3101-3103.

[14] R. Robey, K. To, O. Polgar, M. Dohse, P. Fetsch, M. Dean, S. Bates, *Adv. Drug Deliv. Rev.* **2009**, *61*, 3-13.

[15] a) Y. S. de Boer, A. H. Sherker, *Clinics in Liver Disease* **2017**, *21*, 135-149; b) M. Xu, P. Dong, X. Tian, C. Wang, X. Huo, B. Zhang, L. Wu, S. Deng, X. Ma, *Pharmacol. Res.* **2016**, *110*, 139-150.

[16] a) S. Sudsakorn, P. Bahadduri, J. Fretland, C. Lu, *Curr. Drug Metab.* 2020, 21, 403-426; b) European Agency Medicines. Guideline on the investigation of drug interactions. Available from: https://www.ema.europa.eu/en/documents/scientific-guideline/guideline-investigation-drug-interactions-revision-1_en.pdf.

[17] a) X. He, J. Fang, L. Huang, J. Wang, X. Huang, *J. Ethnopharmacol.* **2015**, *172*, 10-29; b) L. Bai, L. Zhu, B. Yang, L. Shi, Y. Liu, A. Jiang, L. Zhao, G. Song, T. Liu, *Int. J. Biol. Macromol.* **2012**, *51*, 705-709.